

## The effect of red blood cell aggregation on velocity and cell-depleted layer characteristics of blood in a bifurcating microchannel

J. M. Sherwood,<sup>1</sup> J. Dusting,<sup>2,a)</sup> E. Kaliviotis,<sup>2</sup> and S. Balabani<sup>1</sup>

<sup>1</sup>*Department of Mechanical Engineering, University College London, London WC1E 7JE, United Kingdom*

<sup>2</sup>*Division of Engineering, King's College London, London WC2R 2LS, United Kingdom*

(Received 30 March 2012; accepted 27 April 2012; published online 11 May 2012)

Red blood cell (RBC) aggregation is a multifaceted phenomenon, and whether it is generally beneficial or deleterious remains unclear. In order to better understand its effect on microvascular blood flow, the phenomenon must be studied in complex geometries, as it is strongly dependent on time, flow, and geometry. The cell-depleted layer (CDL) which forms at the walls of microvessels has been observed to be enhanced by aggregation; however, details of the characteristics of the CDL in complex regions, such as bifurcations, require further investigation. In the present study, a microchannel with a T-junction was used to analyze the influence of aggregation on the flow field and the CDL. Micro-PIV using RBCs as tracers provided high resolution cell velocity data. CDL characteristics were measured from the same data using a newly developed technique based on motion detection. Skewed and sharpened velocity profiles in the daughter branches were observed, contrary to the behavior of a continuous Newtonian fluid. RBC aggregation was observed to increase the skewness, but decrease the sharpening, of the velocity profiles in the daughter branches. The CDL width was found to be significantly greater, with a wider distribution, in the presence of aggregation and the mean width increased proportionally with the reciprocal of the fraction of flow entering the daughter branch. Aggregation also significantly increased the roughness of the interface between the CDL and the RBC core. The present results provide further insight into how RBC aggregation may affect the flow in complex geometries, which is of importance in both understanding its functions *in vivo*, and utilizing it as a tool in microfluidic devices. © 2012 American Institute of Physics. [<http://dx.doi.org/10.1063/1.4717755>]

### I. INTRODUCTION

Blood is a two phase fluid consisting of formed elements suspended in plasma. The majority of the formed elements are red blood cells (RBCs) at a physiological volume concentration (hematocrit) of approximately 45%. RBCs are highly deformable and have a propensity to aggregate under low shear conditions and in the presence of certain plasma proteins (mainly fibrinogen) or other long chain macromolecules such as Dextran. The combined effects of deformability and aggregation lead to blood having shear thinning characteristics, which are of particular importance in the microvasculature, wherein the flow is dominated by viscous effects. Increased levels of aggregation have been linked with a large number of pathological states, such as sickle cell anemia<sup>1</sup> and diabetes.<sup>2</sup> However, aggregation only occurs in athletic species,<sup>3</sup> which implies that it may have some positive function. According to the opposing depletion and bridging theories of aggregation, an attractive force is generated between two adjacent cells due to either the depletion of macromolecules near the cell surface<sup>4</sup> or due to the

<sup>a)</sup>Present address: Schlumberger Cambridge Research Center, Cambridge CB3 0EL, United Kingdom.

absorption of the same chains of macromolecules from the membrane of a neighboring RBC.<sup>5</sup> Disaggregation occurs when a shear or elongational force applied to the aggregated cells exceeds the binding force. Previous studies of aggregation have provided significant insight into its effects on microvascular blood flow. However, research aimed at elucidating the bulk effect of aggregation on the apparent viscosity in capillary tubes, viscometers, individual vessels, and whole organs have reported differing results. While a number of studies have reported an increase in flow resistance in the presence of aggregation,<sup>6–8</sup> others have observed a counterintuitive reduction in viscosity with increased aggregation levels,<sup>9,10</sup> which has been attributed to phenomena such as network formation in Couette flow<sup>11</sup> and the breakdown of the microstructure in tube flow.<sup>12</sup> As a result, it is still not clear what the overall effect of aggregation on blood flow *in vivo* or in biomicrofluidic devices will be.

On the local scale, it has been shown that aggregation tends to blunt velocity profiles,<sup>6,13</sup> which can increase viscous dissipation and therefore apparent viscosity. However, aggregation leads to syneresis and increased lateral migration, which results in a region of low cell density near the wall, although increased cell-cell interactions (due to increased cell packing) can counter this effect to some extent.<sup>4</sup> This region is interchangeably called the cell-free layer (CFL)<sup>14</sup> or cell depleted layer (CDL),<sup>13</sup> the latter allowing for the fact that cells occasionally pass through this region. In channel flow, the highest shear rates occur adjacent to channel walls. Due to the low cell concentration, the viscosity in the CDL is reduced compared to the cell-rich core. As the location of the CDL is coincident with the region of highest shear rate within the flow, the presence of such a layer can significantly reduce the apparent viscosity. However, it has been shown that a rough interface between the cell-rich core and the CDL can result in increased viscous dissipation, as cells protrude into the CDL.<sup>15,16</sup> This has the effect of increasing the effective viscosity of the CDL and hence reduces the extent to which its presence reduces apparent viscosity. As well as being dependent on aggregation, the width of the CDL is also affected by hematocrit, RBC deformability, vessel diameter, flow rate, the presence (or absence) of the endothelial glycocalyx layer, and the amount of time allowed for the CDL to form.<sup>17–19</sup> Historically, the CDL was measured manually from images by a human observer.<sup>8,17</sup> Kim *et al.*<sup>20</sup> suggested a method based on binary thresholding of images using Otsu's method. This was later compared with other thresholding methods<sup>16</sup> and a method based on the gradient of the intensity.<sup>21</sup> These methods require an analysis line to be defined and only provide data at a single axial location. This location is chosen in a region where the vessel wall is clearly defined and the contrast between the cell core and surrounding regions is high, i.e., the analysis is carried out at a single location and is not applicable to an entire flow field, although it can be carried out at multiple locations.

The effects of aggregation have generally been studied in straight vessels or capillary tubes in order to limit variability in the measurements and simplify the analysis. However, in the vasculature, vessels regularly bifurcate, which leads to non-uniform velocity and cell distributions. Thus, the effects of aggregation in more complex geometries require further elucidation. At microvascular bifurcations, the non-uniform hematocrit distribution can lead to the branch with a lower proportion of the flow receiving disproportionately fewer cells, in an effect known as plasma skimming. Bifurcating microchannels, representing microvascular bifurcations, have been used in the past to investigate this phenomenon.<sup>22–24</sup> In these experiments, bulk measurements of hematocrit and flow rate were used to quantify the plasma skimming phenomenon. Fenton *et al.*<sup>24</sup> identified the most important parameters as being parent vessel hematocrit, tube diameter and flow ratio (the proportion of the flow from the parent branch entering a given daughter branch), although aggregation was absent in their study due to the high shear present at the flow rates utilized. It has been observed that aggregation increases plasma skimming.<sup>25,26</sup> This is probably a result of aggregation enhancing the CDL width, as the presence of a CDL accounts for the majority of the plasma skimming effect on the scales considered in these studies.<sup>27</sup> However, detailed descriptions of the flow field around the bifurcation have not been reported in microscale bifurcation studies, with a few exceptions. A recent study by Leble *et al.*<sup>28</sup> considered a bifurcating and converging microchannel, with an angle between the daughter branches of 60°, and described velocity profiles using particle tracking velocimetry

(PTV). Their velocity data showed little deviation from predicted Newtonian distributions and they qualitatively observed a cell-depleted region. However, the effect of flow ratio was not considered as their geometry resulted in an equal split between the branches. Ishikawa *et al.*<sup>29</sup> also reported PTV data in a similar geometry. Chesnutt and Marshall<sup>30</sup> simulated aggregating blood flow in a bifurcation, but found that aggregation did not influence plasma skimming as particles followed their streamlines. Detailed quantitative experimental descriptions of the effect of flow ratio, aggregation, and the CDL around bifurcations are still required, as these factors affect blood rheology significantly. While PTV provides an accurate Lagrangian description of the velocities of individual cells, it is limited in its capability to provide Eulerian data on the whole flow field. Extracting such information from PTV data requires averaging over a large number of cells, and hence time period, and results in relatively low spatial resolution and a certain degree of inherent scatter. As an alternative, micro-particle-image velocimetry ( $\mu$ PIV) can provide very high spatial resolution, full flow field data with a significantly greater degree of accuracy, and has been used extensively in recent years to improve understanding of blood flow.<sup>31–33</sup>  $\mu$ PIV is an image based method in which two images are acquired in quick succession, and then segmented into interrogation windows (IW). Each IW is then correlated between the two images to help obtain a best estimate of the velocity within that IW. In order for a single, accurate correlation peak to be obtained, the image must have features that trace the flow and can be correlated in the two images. This is normally achieved by seeding the flow field with fluorescent particles which are excited with a laser.<sup>34</sup> In the case of blood flow, it has been shown that brightfield illuminated RBCs can also provide suitable images for correlation.<sup>35,36</sup> Furthermore, these images can be further analyzed to provide additional information on the aggregation behavior and viscosity fields.<sup>37,38</sup>

Blood samples are regularly analyzed in clinical and scientific settings for diagnostic and research purposes, but traditional approaches often require large samples and extensive labor and equipment investment. Microfluidic technologies are increasingly being utilized as an alternative tool due to their many advantages, such as small sample size, disposability, flexibility, etc. For example, such devices have been used for separating viruses,<sup>39</sup> stem cells,<sup>40</sup> cancer cells,<sup>41</sup> and plasma<sup>42–45</sup> from blood samples. Many of these devices use the two-phase nature of microvascular blood flow and bifurcating geometries to enhance separation, but the influence, and possible benefit of RBC aggregation has generally been overlooked, despite evidence that it enhances phase separation<sup>26</sup> and increases leukocyte margination.<sup>46</sup> Kuczenski *et al.*<sup>47</sup> found that RBC aggregation caused flow control problems in their device, which was developed for separating *Escherichia coli* from blood cells, and suggested that aggregation should be avoided/eliminated. It is possible, however, that the margination of white blood cells, platelets, or hardened RBCs, and/or the phase separation caused by RBC aggregation, could be utilized in novel designs of biomicrofluidic devices. For such an application, aggregation properties in microfluidic devices must first be better understood.

In the present study, detailed information on the velocity fields of the RBCs and the characteristics of the CDL are described. Both aggregating and non-aggregating blood are analyzed in a bifurcating microchannel in order to improve understanding of the effects of aggregation on flow fields in complex geometries. An alternative methodology for CDL measurement is proposed, which uses a standard deviation (SD) image calculated from a series of images to sense movement of the suspended phase, and can provide information on the CDL distribution for a whole flow field. Temporally and spatially averaged velocity profiles are considered for a range of flow ratios and their characteristics are analyzed with regards to the CDL and other flow properties. The effects that aggregation has on these data provide further insight into its role in the microvasculature.

## II. MATERIALS AND METHODS

### A. Sample preparation

The study was approved by the South East London Research Ethics Committee (Ref. :10/H0804/21) and informed consent was obtained from volunteers. Human blood was acquired

from a healthy volunteer into vacuum tubes preloaded with 1.8 mg/ml EDTA to prevent coagulation. The RBCs were separated via centrifugation and washed twice in phosphate buffered saline (PBS). They were then re-suspended in PBS at a hematocrit of 25%. Although systemic hematocrit is around 45% under physiological conditions, microvascular hematocrit is reduced due to the Fåhræus effect. For example, Særelius and Duling<sup>48</sup> found that local hematocrit was reduced to around 0.6 times the systemic hematocrit in arterioles of diameter close to the hydraulic diameter of the channel used in the present study. Hence, for a channel of this size, a hematocrit of 25% can be considered to be physiological. For the aggregating cases, Dextran 2000 was added at a concentration of 5 g/l. The high molecular weight and low concentration of Dextran was chosen so that two important aggregation characteristics, namely the aggregate morphology<sup>52</sup> and aggregation kinetics, approximate those within the range of normal blood samples.

## B. Acquisition system

A schematic of the experimental setup is shown in Figure 1(a). The SU8 microchannel (Epigem, England) consisted of a straight section ( $\sim 50$  mm) followed by a T-junction (Figure 1(b)). The channel had width  $w = 100\ \mu\text{m}$ , depth  $d = 40\ \mu\text{m}$  and was connected via short polytetrafluoroethylene (PTFE) tubes of internal diameter 0.5 mm to inlet and outlet reservoirs. The inlet reservoir was sealed and the pressure acting on the fluid was monitored and controlled using a pressure system with manual and stepper motor actuated needle valves, for coarse and fine control, respectively, connected to a compressed nitrogen cylinder. This system allowed control of the inlet pressure over the range 0–50 kPa with a resolution of  $\sim 10$  Pa. A magnetic stir bar was used to allay the effects of aggregation and sedimentation in the inlet reservoir. By independently adjusting the height of the outlet reservoirs using micrometer stages, the distribution of flow between the two daughter branches (flow split) could be controlled through applying a hydrostatic pressure difference. The flow system was mounted on the stage of an inverted microscope (Leica DM ILM, Germany), with the focal plane set to the center of the channel, as indicated in Figure 1(a) (inset) and illumination was provided using a 100 W halogen light source. All acquisition and control were carried out using LabVIEW (National Instruments).

## C. Experimental protocol

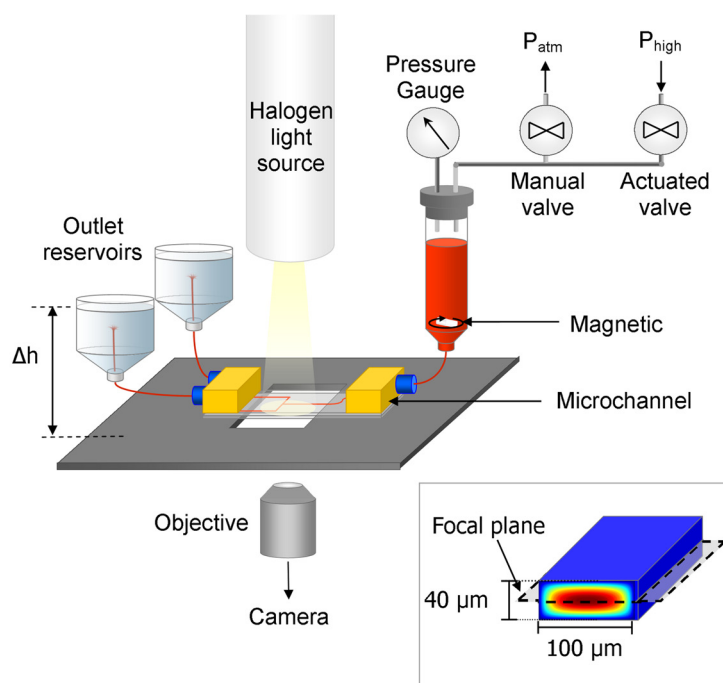
In order to ensure that the sample was disaggregated and uniformly distributed before acquisition, the inlet pressure was set to a high value. The flow split was set by adjusting the height of the two outlet reservoirs up and down in equal proportions, keeping the overall pressure drop approximately constant. Prior to acquisition, the stirrer was turned off to avoid vibrations and the pressure was reduced over a period of 5 s and then held constant at a desired value. Acquisition of 2000 images at a frame rate of 250 Hz was triggered 20 s later, allowing time for the hematocrit and aggregation states in the channel to become uniform. For each case (PBS and Dextran treated samples), 35 data sets were acquired at a range of flow splits. All experiments were carried out at room temperature. The flow rate in the parent branch was  $Q_p \approx 3.5 \pm 0.5\ \mu\text{l/h}$ . This gave a mean parent branch velocity around 0.25 mm/s, which would represent a reduced flow environment for an arteriolar bifurcation of this scale, and could hence be considered to represent a pathological flow rate.

## D. Image processing

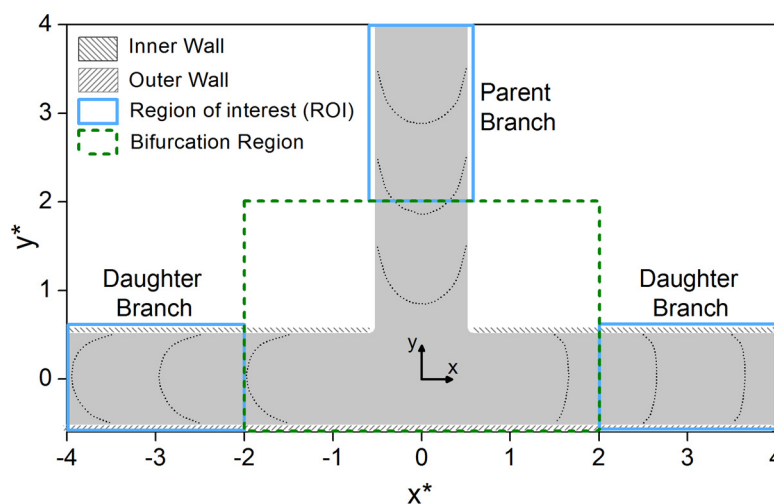
The images were pre-processed so that the channel was at the same location (relative to the image) in each data set. This involved identifying the location of the channel walls using the standard deviation of each pixel in a stack of images and cropping to leave branches of  $3.5w$  in length. Figure 1(b) shows a schematic of this region, along with the co-ordinate system; co-ordinates have been normalized by the channel width,  $x^* = x/w$  and  $y^* = y/w$ .

### 1. Particle image velocimetry

Multi-pass ensemble averaged PIV processing was carried out on each of the data sets, providing a final window size of  $8 \times 8$  pixels and a vector spacing of 4 pixels ( $2.63\ \mu\text{m}$ ) using JPIV.



(a)



(b)

FIG. 1. (a) Schematic of the experimental setup. Inset: cross sectional area, analytical velocity distribution, and focal plane. (b) Geometry of the imaging area. The coordinate system and terminology used are indicated.  $x^*$  and  $y^*$  are normalized relative to the channel width,  $w$ . Sample velocity profiles are included from the Dextran case with 75:25 flow split.

The images were combined into 180 pairs with a time separation of 8 ms spanning the 8 s acquisition period. The resulting vector fields were filtered using a normalized median test<sup>49</sup> and invalid vectors were replaced with the median of the surrounding vectors. For the estimation of the flow rate for each branch, the spatially averaged velocity profiles were acquired in the regions indicated by the region of interest (ROI) in Figure 1(b).

As a result of blurring near the channel walls, the two IW next to the wall were not able to produce valid vectors. In order to calculate the mean velocity,  $U$ , it was necessary to make an assumption about the velocity at the walls. The simplest assumption to make was to take the



velocity at the wall to be equal to zero; although this may not strictly be the case, as will be discussed later. A spline fit was then used to interpolate the missing vectors. The parent branch flow rate was estimated using  $Q_p = U' A$ , where  $U'$  is the mean velocity corrected by scaling experimental values to account for the difference between the mean velocity in the center plane and that for the whole channel. The scaling factor was calculated using the analytical solution<sup>50</sup> and was found to be 0.6672, hence  $U' = 0.6672U$ . The flow ratio is defined as  $Q^* = Q_d/Q_p$ , where the subscripts  $d$  and  $p$  represent parent and daughter branches, respectively. As the cross sectional area was the same in all branches, this was calculated according to  $Q^* = U_d/U_p$ .

## 2. Cell-depleted layer analysis

Sample images of the RBCs flowing through the bifurcation region are shown in Figure 2 for the Dextran and PBS cases. Previous methods of identifying the CDL reported in the literature were not suitable for these brightfield illuminated images, as the blurring at the wall and the non-linearity between the local hematocrit and the image intensity precluded analysis based on static images. Thus, a new algorithm was developed and is shown schematically in Figure 3. The approach, implemented in LabVIEW, is based on motion detection using a SD image in which the intensity at each pixel location is given by the temporal standard deviation across a series of images. Using this motion detection method allows identification of the layer location even within the blurred region. However, due to the large difference in flow rates in different branches, the method is sensitive to the cell flux. To improve accuracy, the number of images in each series (from which the SD was derived) was selected based on *a priori* knowledge of the flow rate in each branch calculated from the PIV, so that the average cell flux was

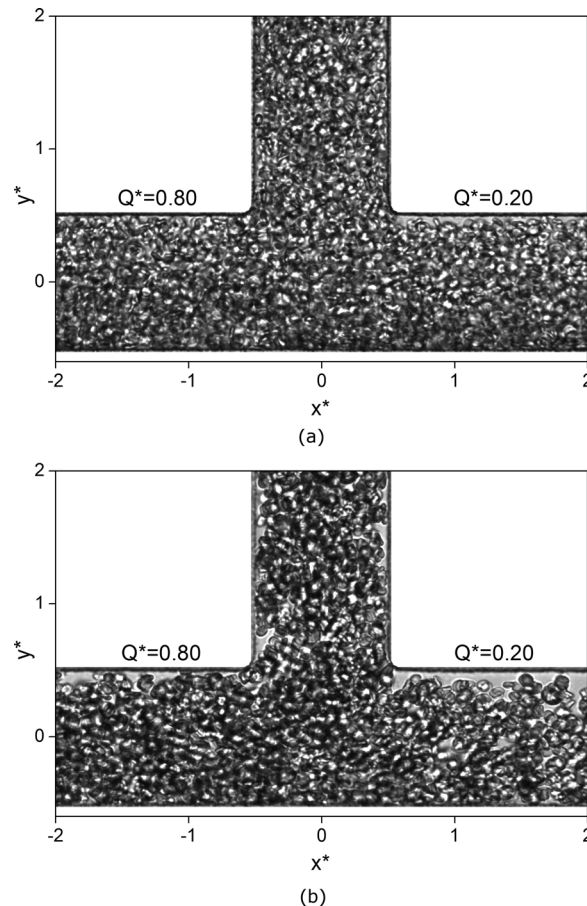


FIG. 2. Sample images of the RBCs in the bifurcation region. (a) PBS case, (b) Dextran case.

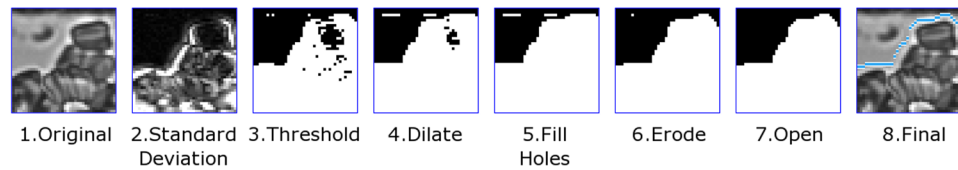


FIG. 3. Schematic of the stages of image processing in the CDL location algorithm.

comparable in each branch. A binary threshold was applied to the SD image. In order to obtain consistent results, it was necessary to use a single threshold for all the data. Thus, the location of the valley between the pixel distributions corresponding to the foreground and background on the histogram was found for a number of cases and the modal value was chosen.

Subsequently, a number of filtering operations were applied. For features which are parallel to the flow direction, the SD may be low, forming a gap, as can be seen in Figure 3. Basic morphological operations were used in order to resolve this problem. The SD image was dilated in the direction of the flow to “bridge” the gap. The holes were then filled and the image was eroded to counteract the dilation. An additional pixel of erosion was applied to undo the blurring effect of the SD image in the flow direction. Finally, an opening function was applied to remove noise. The distance between the channel wall and the CDL at each location perpendicular to the channel wall was then defined as the CDL width, as can be seen in the final panel of Figure 3. To validate the method, manual measurements at 40 locations were compared to those calculated by the algorithm. The absolute residual differences had a mean and standard deviation of  $\sim 1$  pixel. The CDL at the outer wall was generally negligible, except at very low flow ratios in the aggregating case. Further specialization of the processing algorithm would be required in order to reliably measure this region due to the very low velocities at the outer wall; therefore, only the CDL at the inner wall of the bifurcation was considered in the present study.

### E. Numerical modeling of flow field

In order to aid interpretation of the observed results, computational fluid dynamics (CFD) simulations using Newtonian and non-Newtonian fluids (Carreau-Yasuda model, parameters from Gijzen *et al.*<sup>51</sup>) were carried out using ANSYS-CFX 13.0. A model of the imaging area, but with branch lengths of  $10w$ , was created and meshed with elements of  $2 \times 2 \times 2 \mu\text{m}$ . Convergence was considered when all residuals were below  $10^{-4}$ . Constant velocity input and a number of different constant pressure outputs were applied such that a range of flow ratios were considered for a single parent branch pressure. The profile in the center plane of the parent branch prior to the bifurcation was compared to the analytical solution<sup>50</sup> and the mean difference was found to be 0.88%.

## III. RESULTS

Sample brightfield illuminated images of the bifurcation region for an 80:20 split of flow between the daughter branches are shown in Figure 2. In Figure 2(a), the cells suspended in PBS are not aggregated and are distributed fairly homogeneously throughout the channel; it can be seen that there are fewer cells at the inner wall compared to the outer wall, particularly in the low flow rate branch. Figure 2(b) shows an equivalent image for the Dextran case. There are clumps and linear rouleaux at various orientations clearly visible throughout the domain. Through the analysis of videos of the Dextran samples travelling through the bifurcation, it was observed that aggregates exist in a range of sizes, from around 2–10 cells per aggregate. The region of low local hematocrit near the inner wall is enhanced in the presence of aggregation and there are visible gaps throughout the channel.

### A. Flow field

The time-averaged flow fields for 50:50 and 80:20 flow splits are shown in Figure 4 for the PBS case. At this scale, the Dextran cases were not qualitatively different and are hence not

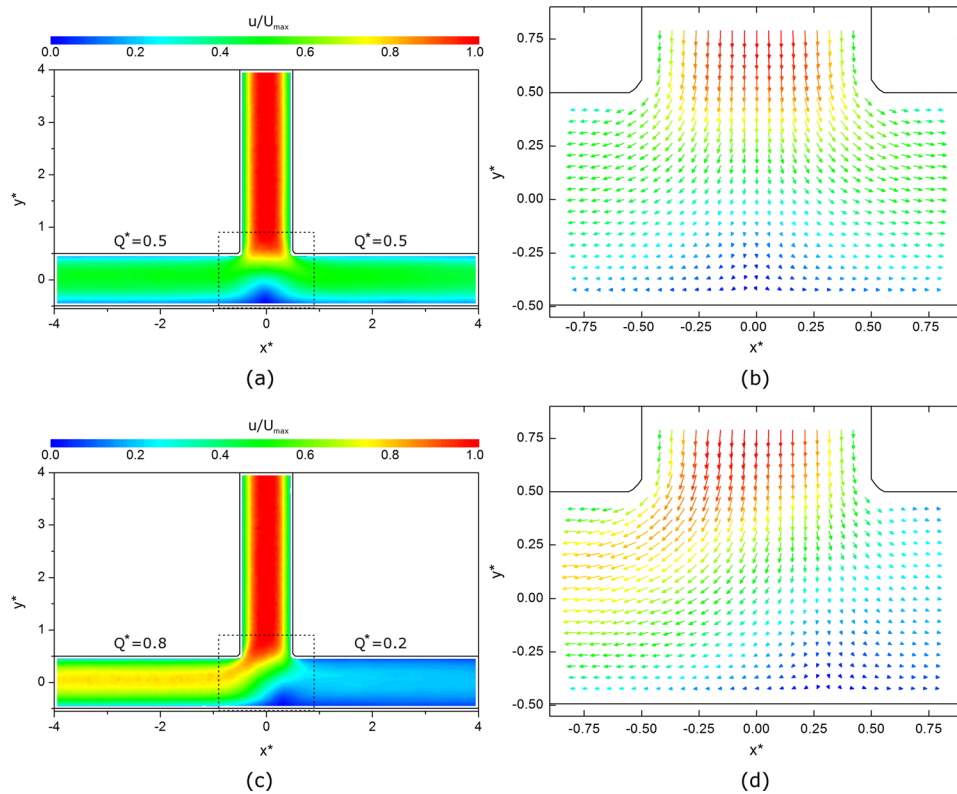


FIG. 4. (a) and (c) RBC velocity magnitude contour plots from PIV data for 50:50 and 80:20 flow splits, respectively. The dashed lines indicate region shown in (b) and (d): Vector fields in the region immediately around the bifurcation. Every other vector is omitted for clarity.

shown here for brevity. The velocity magnitude at each location,  $u$ , is normalized relative to the maximum velocity for each case,  $U_{\max}$ . Figures 4(a) and 4(c) show velocity magnitude contour plots for the whole domain. For both flow splits, a blunted parabolic shape can be observed in the parent branch (see also Figs. 1(b), 4(b) and 4(d)), as would be expected in a high aspect ratio rectangular channel. As the flow enters the bifurcation region, the velocity rapidly decreases toward the stagnation point, which is centrally located for the 50:50 flow split, but offset towards the low flow branch for the 80:20 split. This can be seen more clearly in the vector plots in Figures 4(b) and 4(d). No flow separation at the vertices of the bifurcation is observed, since the Reynolds number is low and the flow is dominated by viscous effects.

In the daughter branches, it can be seen that the lateral velocity component rapidly diminishes and a relatively constant velocity distribution is established by around  $x^* = \pm 1$ . Finally, it should be noted that this profile can be observed to be slightly skewed towards the inner wall of the channel for all  $Q^*$  (see also Fig. 1(b)).

Sample velocity profiles, spatially averaged over the ROI, are presented in Figure 5 at  $Q^* = 0.56$ .  $U^*$  is the velocity normalized with the mean velocity  $U$ . As an estimate of the error involved in the averaging procedure, the mean coefficient of variation for each lateral position for all data sets was found to be 1%–2%.

Due to the skewed nature of the profile, previously defined equations<sup>6,53,54</sup> could not be used to characterize the velocity profiles. Additionally, the velocity measurements near the walls measured using the RBCs as tracers were not zero due to the inherent difficulties in obtaining accurate profiles near the wall of a channel and the rolling of the cells along the vessel wall. Thus, any proposed equation must allow for bluntness, skewness, and the slip velocity at each wall. Due to the complexity in defining such an equation in which the parameters are independent, a 4th order polynomial fit was used to smooth the data. The bluntness,  $B$ , can then



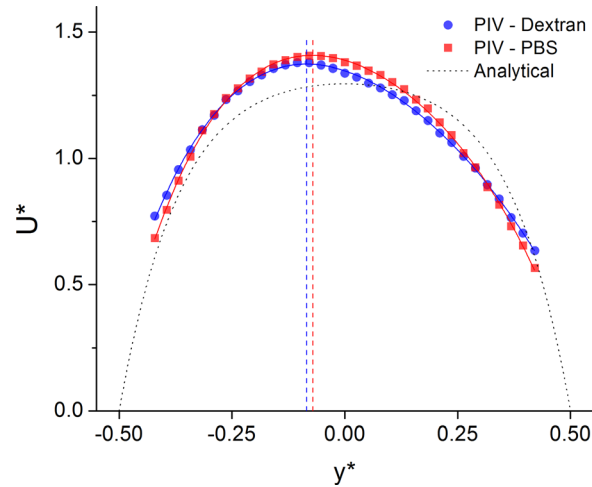


FIG. 5. Sample averaged velocity profiles for Dextran and PBS cases at  $Q^* = 0.56$ . Solid lines represent fourth order polynomial fit. Dotted black line shows the analytical solution. Dashed vertical lines show location of maximum velocity. Dextran:  $B^* = 0.94$ ,  $S^* = 8.5$ . PBS:  $B^* = 0.92$ ,  $S^* = 7.1$ .

be defined as  $B = U/U_{\max}$  where  $U$  is the average velocity having assumed the no-slip condition at the wall. Such an assumption may introduce errors, but is necessary for this analysis to be applied.  $B$  is normalized with the value of  $B_N$  obtained from the analytical solution for a Newtonian fluid,<sup>50</sup> hence  $B^* = U/U_{\max}B_N$ .

The skewness,  $S^*$ , is defined as the distance between the location of maximum velocity and the centerline of the channel and is presented as a percentage of the channel width. As can be seen in Figure 5, the Dextran sample is marginally blunter and more skewed than the PBS sample. However, both are less blunt than the Newtonian solution, indicated by the dotted black line in the figure.

The bluntness,  $B^*$ , of the velocity profiles measured for different flow ratios is considered in Figure 6. Data for  $Q^* < 0.1$  are omitted, as the flux was not sufficient to obtain representative time averaged data. Additionally, outliers, considered as values more than two standard deviations from the mean, were removed. The average bluntness in the parent branch for each case is indicated by a dashed line. For the Dextran case, the bluntness is not significantly different from the Newtonian; however, for the PBS case the profiles are sharper (less blunt). Overall, it can be seen that the bluntness in the daughter branches is greater in the Dextran case.

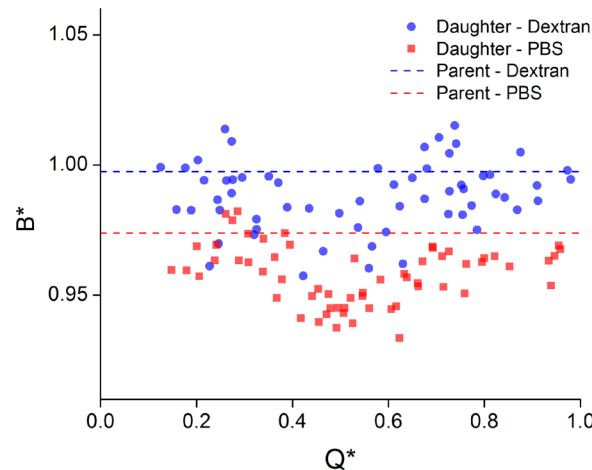


FIG. 6.  $B^*$  against  $Q^*$  for Dextran and PBS cases. Dashed lines show mean values in parent branch.

TABLE I. Probability that the correlation coefficient is significant,  $P$ , for bluntness,  $B^*$ , corresponding to Figure 6 and skewness,  $S^*$ , corresponding to Figure 7.

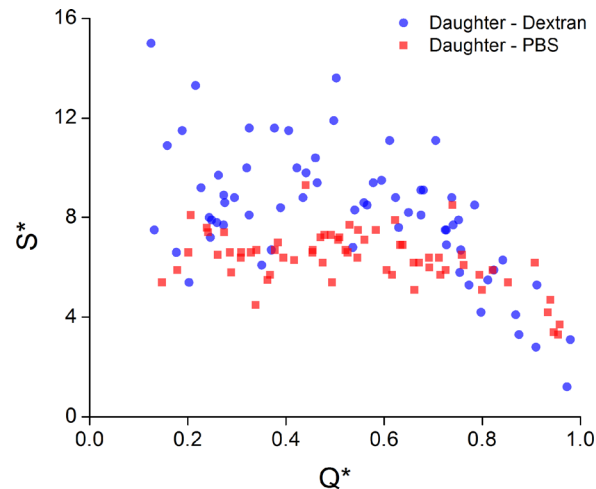
	$B^*, Q^* < 0.5$	$B^*, Q^* > 0.5$	$S^*, Q^* < 0.5$	$S^*, Q^* > 0.5$
Dextran case	0.0546	0.0524	0.7395	$< 10^{-6}$
PBS case	0.0003	0.0001	0.6533	$< 10^{-6}$

Considering the bluntness in the daughter branch, at  $Q^* = 1$ , one would expect  $B^*$  to be equivalent to the parent branch, as the effective geometry becomes a simple  $90^\circ$  corner and, in the absence of inertia, the profile in the high flow daughter branch should therefore be close to that of the parent branch. This seems to be the case for both Dextran and PBS cases. Figure 6 illustrates that in the low flow branch ( $Q^* < 0.5$ ), the bluntness decreased with increasing  $Q^*$ , while in the high flow branch ( $Q^* > 0.5$ ) the bluntness increased with increasing  $Q^*$ . As  $Q^* = 0.5$  indicates the transition from high to low flow branch, and due to the symmetry and clear trends observed in Figure 6, the data will be henceforth analyzed in terms of whether they are greater or less than  $Q^* = 0.5$ . Using this approach, the significance of the observed trends can be considered using the probability that the correlation coefficient is significant,  $P$ , as summarized in Table I. For the PBS case, the trends are very significant. For the Dextran case, the  $P$ -value is just slightly above the often used significance value of 0.05, but is close enough to be considered significant.

The skewness of the velocity profiles,  $S^*$ , is considered in a similar manner in Figure 7. As with the bluntness, for  $Q^* = 1$ , one might expect negligible skewness, as was observed in the parent branch. This general trend is observed in both Dextran and PBS cases. For the high flow branch ( $Q^* > 0.5$ ), both cases showed a trend of increasing skewness as  $Q^*$  decreased from 1 to 0.5, which was highly significant (see Table I). For the low flow branch ( $Q^* < 0.5$ ), there was no significant relationship between skewness and flow ratio for either case. Hence, the mean skewness is considered, and was calculated to be 9.3% and 6.6% for the Dextran and PBS cases, respectively.

## B. Cell-depleted layer characteristics

The CDL measurement methodology applied in the present study allows detailed analysis of the CDL characteristics in both time and space. The CDL width ( $\delta$ ) was normalized by the channel width,  $w$ , such that  $\delta^* = \delta/w$ . Figure 8(a) shows the instantaneous profile of  $\delta^*$  along

FIG. 7.  $S^*$  against  $Q^*$  for Dextran and PBS cases.

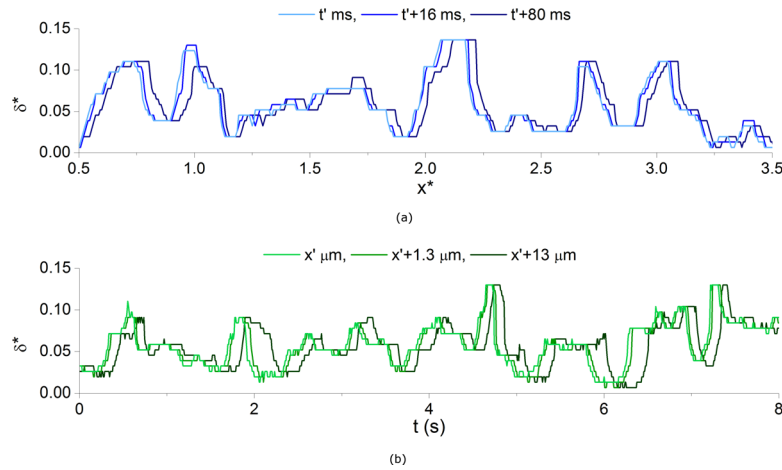


FIG. 8. CDL width in space and time for Dextran case,  $Q^* = 0.25$ . (a) Instantaneous CDL along the daughter branch at three points in time, relative to  $t' = 2$  s, (b) variation in CDL in time at three locations, relative to  $x' = 3.5x^*$ .

the inner wall of the daughter branch for the Dextran case for  $Q^* = 0.25$  at three moments in time. It can be observed that the profile at  $t'$  changes very little for  $t' + 16$  ms and is simply convected downstream. For  $t' + 80$  ms the profile is similar but has altered slightly and advanced further downstream, although by different amounts at different locations. Figure 8(b) shows the temporal distribution of CDL width at three points in space for the same case. It can be seen that at each location,  $\delta^*$  exhibits roughly the same fluctuations, with a phase shift dependent on the position in the channel. Hence, despite the fact that at a given moment in time there is a large variability in the CDL width, its overall distribution will be relatively consistent in time.

To further consider the behavior of the CDL, probability distributions of  $\delta^*$  at each location in space are considered in Figure 9 for selected flow ratios. For the Dextran case (Fig. 9(a)),  $\delta^*$  is significantly increased in comparison to the PBS case (Fig. 9(b)), and a wide distribution is observed. For  $Q^* \geq 0.5$ , the probability of  $\delta^*$  is greatest along the channel wall and decreases towards the center of the channel. At  $Q^* = 0.25$ , the modal width is observed at a position offset from the channel wall and the spread of the distribution is greatly increased. At  $Q^* = 0.1$ , these trends are exaggerated further, with maximum CDL widths as great as 25% of the channel width. For the PBS case (Fig. 9(b)), the CDL distributions are significantly narrower. For  $Q^* \geq 0.5$ , the modal CDL width is at, or very close to, the wall. At  $Q^* = 0.1$ , the modal width moves away from the wall immediately after the bifurcation, then approaches the wall at around  $x^* > 2.5$ . For  $Q^* = 0.25$ , this movement away from the wall is also present, but is less pronounced, and the mode returns to the wall when  $x^* = 2$ . It is worth reiterating that the shape is not a result of flow separation, and thus must be due to the interactions of the RBCs with local hydrodynamic forces or other cells.

The distribution of the CDL is considered further in Figure 10, which shows stacks of probability distribution functions (PDFs) of the normalized CDL width ( $\delta^*$ ) averaged along the ROI (in the axial direction),  $\Delta^*$ , for both the Dextran and PBS cases. At high flow ratios (blue), the modal CDL width is at, or close to zero for both Dextran and PBS cases. For the latter, the position of the modal CDL width does not move significantly away from the channel wall, but the distribution becomes slightly more spread out as  $Q^*$  decreases. For the Dextran case, the position of modal CDL width moves away from zero as  $Q^*$  decreases from 0.5, and the distribution becomes steadily flatter and broader as the flow ratio decreases, with a modal value of around 10% of the channel width for very low flow ratios.

The roughness of the CDL is an important parameter as it will affect the temporal characteristics and magnitude of the shear stress developed at the wall, and therefore it is prudent to consider how the width of the CDL affects its roughness; this was quantified using the axially

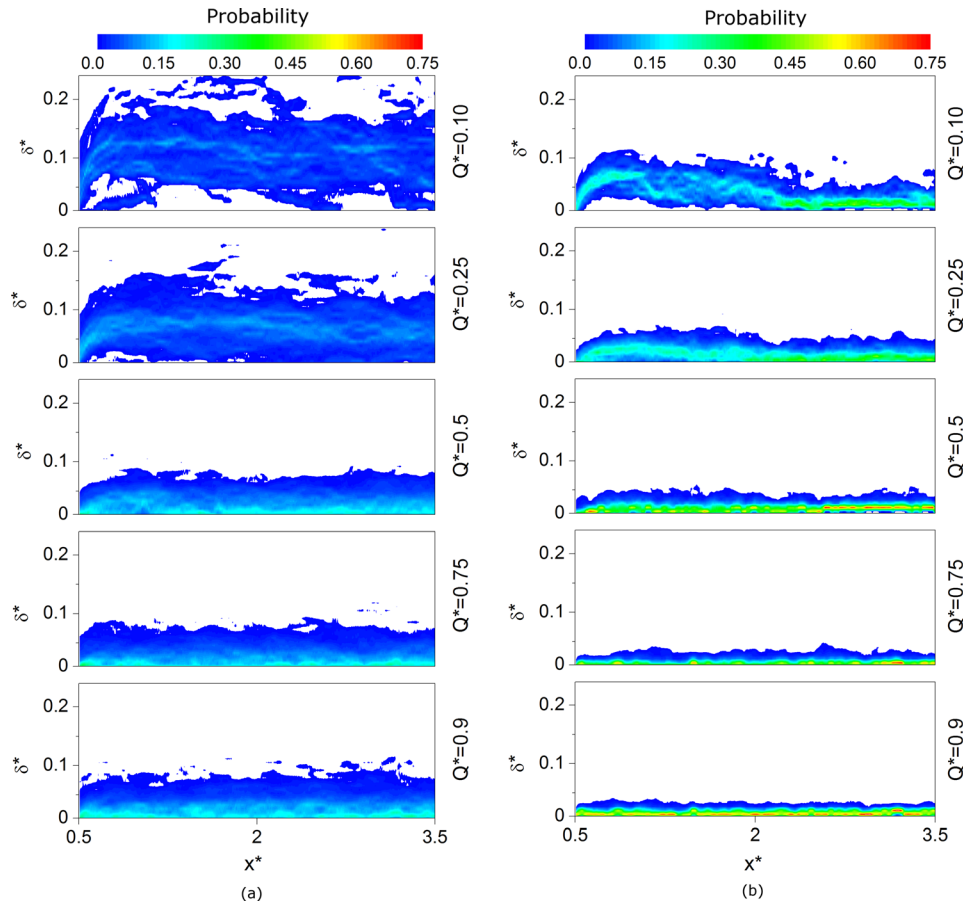


FIG. 9. Probability distributions for normalized mean CDL width in the daughter branch at a selection of flow ratios for (a) Dextran case and (b) PBS case. The horizontal axis is normalized distance from the bifurcation and the vertical axis is the normalized CDL width. Contours indicate probability that the edge of the cell-depleted layer will be of a certain width for each axial location. White regions indicate no occurrences of CDL edge at that width and location.

averaged (in the ROI) temporal standard deviation of the CDL, normalized with respect to the channel width such that  $\sigma^* = \sigma/w$  as shown in Figure 11 for the daughter and parent branches. The bar symbols on  $\bar{\Delta}^*$  and  $\bar{\sigma}^*$  are used to indicate values averaged in the lateral direction to give a mean value for each  $Q^*$ . Although the distributions are strongly non-normal, the standard

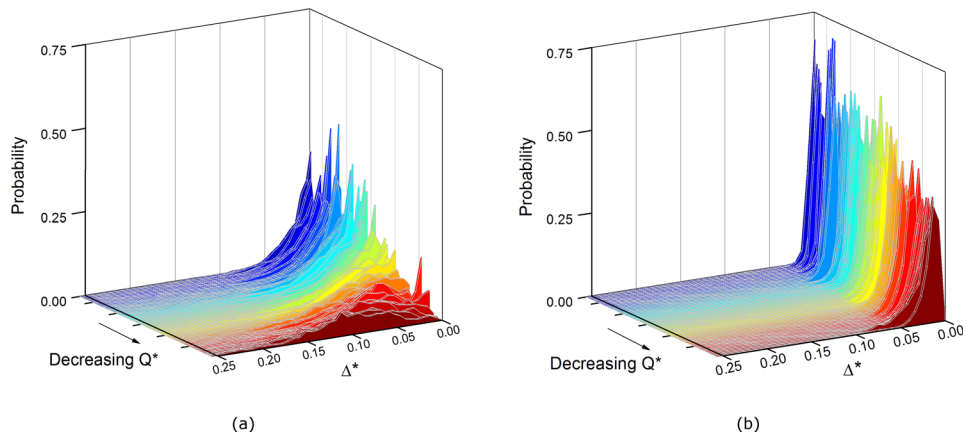


FIG. 10. Probability distributions for spatially averaged (in the ROI), normalized mean CDL width,  $\Delta^*$ . The stacks are ordered in terms of decreasing flow ratio, with blue representing high  $Q^*$  and red representing low  $Q^*$ . (a) Dextran, (b) PBS case.

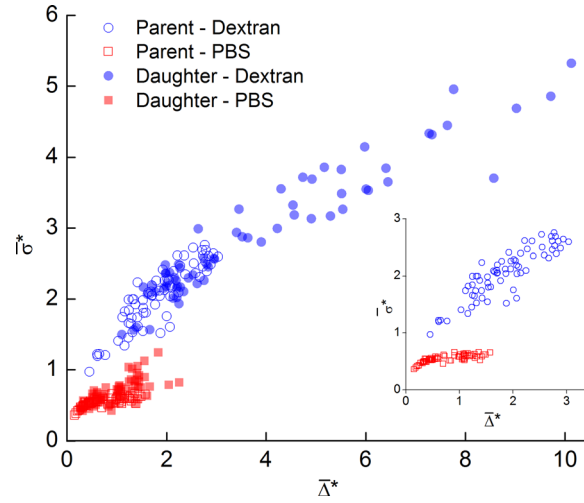


FIG. 11. CDL roughness indicated by comparing normalized standard deviation of CDL width against mean  $\Delta^*$ . The inset shows parent branch only, for comparison with straight channel/vessel studies.

deviation and mean CDL are commonly used to consider the characteristics of the CDL<sup>55–57</sup> and so are utilized here. The inset in Figure 11 shows the values in the parent branch, considered to be the steady state results. As  $\bar{\Delta}^*$  increases, the roughness,  $\bar{\sigma}^*$ , in the PBS case increases only slightly, whereas for the Dextran case, the roughness increases steadily with the mean width. This trend is continued further in the daughter branches as can be seen in Figure 11. The spatial standard deviation showed very similar trends (omitted here for brevity), since the temporal and spatial signals are strongly coupled, as can be seen in Figure 8.

The impact of the flow ratio on the average width of the CDL is considered in Figure 12(a). The solid lines show the mean  $\bar{\Delta}^*$  in the parent branch. In the Dextran case,  $\bar{\Delta}^*$  was roughly doubled in the parent branch from 0.8% to 1.8% of the channel width, although as can be seen in the inset of Figure 11,  $\bar{\Delta}^*$  was broadly distributed. In the PBS cases, the mean  $\bar{\Delta}^*$  increased slightly as the proportion of flow entering the daughter branch decreased. However, for the Dextran case, the mean  $\bar{\Delta}^*$  increased significantly with decreasing  $Q^*$ , reaching approximately 10% for low flow ratios. It should be noted that the maximum instantaneous CDL width was as large as 45% for  $Q^* = 0.1$  in the Dextran case.

For a given CDL width in the parent branch,  $\bar{\Delta}_p^*$ , if the cells exactly followed their streamlines, the CDL width in the daughter branch,  $\bar{\Delta}_d^*$  would increase in proportion to  $1/Q^*$

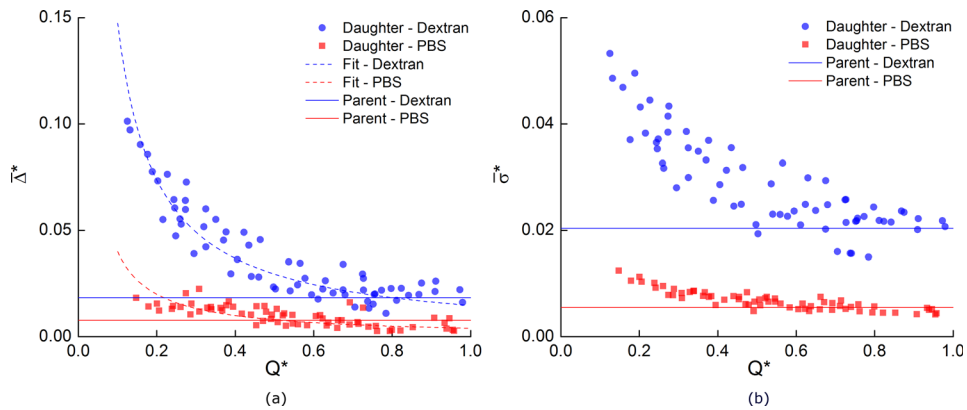


FIG. 12. Effect of flow ratio on CDL characteristics. Solid lines represent mean values in parent branch. (a) Mean  $\Delta^*$ . Dashed lines show fits to Eq. (1), solid lines show average value in parent branch. (b) Normalized standard deviation of CDL width. Solid lines show average value in parent branch.



(assuming 2D flow). Deviations from this idealized situation, indicating movement of the cells away from their streamlines, can be accounted for using a constant of proportionality  $\alpha$ . Thus, the data are fit to the equation

$$\bar{\Delta}_d^*(Q^*) = \alpha \bar{\Delta}_p^*/Q^* \quad (1)$$

by minimizing the mean square error. The coefficient  $\alpha$  then indicates the extent of deviation from the idealized situation. The fits are shown as dashed lines on Figure 12(a).

Finally, Figure 12(b) shows how the roughness (SD) of the CDL was affected by aggregation and  $Q^*$ . It can be seen that the roughness increased as the flow ratio decreased, and that aggregation enhanced this effect significantly.

## IV. DISCUSSION

### A. Velocity profiles

Two key results reported above are the effect of flow ratio on the velocity profiles and CDL characteristics, and the amplifying effect of aggregation. Given the images shown in Figure 2, it is clear that there is aggregation present in the Dextran case and that the cells are not aggregated in the PBS case. Therefore, the following discussion will treat the Dextran case and the presence of aggregation as synonymous.

In the CFD simulations, for both Newtonian and Carreau-Yasuda viscosity models, the skewness was zero within around one channel width of the bifurcation region for all flow ratios. While the velocity profile reached a steady shape in a similar distance in the experimental data, the skewness persisted downstream. Thus, it is clear that the skewness observed in the velocity profiles of the RBCs in Figures 5 and 7 is predominantly a result of the two-phase nature of the flow and not the shear-dependent characteristics of blood.

The presence of the CDL results in reduced viscosity near the inner wall of the daughter branch. For a two dimensional parallel pressure driven flow of two immiscible fluids of different viscosities, the velocity profile becomes skewed towards the region of low viscosity. This suggests that the existence of the CDL may be partly responsible for the observed skewness. A comparison of Figure 12 with Figure 7 shows that as  $Q^*$  decreases, both  $\delta^*$  and  $S^*$  increase. Furthermore, it is commonly reported that, in addition to the CDL, there will be an asymmetric hematocrit distribution downstream of an arteriolar or microchannel bifurcation.<sup>4,58</sup> Das *et al.*<sup>59</sup> showed that skewed viscosity profiles can result in skewed velocity profiles. This phenomenon is probably involved in the present data and requires further analysis.

Leble *et al.*<sup>28</sup> recently reported a comparison of simulated Newtonian flow through a Y-bifurcation with PTV data from labeled RBCs. They observed similar profiles in both cases and the skewness appeared to diminish rapidly after the bifurcation. However, the flow rate was higher ( $\sim 12 \mu\text{l/h}$ ) and the hematocrit was lower (14%) in their study compared to the data reported here, and flow ratio was not considered. It is also not clear whether the resolution in their velocity measurements was sufficient to pick up the subtle skewing observed here, which would likely be reduced in their Y-bifurcation geometry.

It is also apparent from the results in Figures 5–7 that aggregation had an influence on both the bluntness and skewness in the daughter branches. Aggregation increased the bluntness of the velocity profile by approximately 2.5% in the parent branch compared to the PBS case ( $P < 0.0001$  from two-tailed  $t$ -test), and this trend continued for all flow ratios in the daughter branches. The skewness was also increased by a larger proportion in the Dextran samples for the lowest flow ratios (Figure 7). Nevertheless, the difference between PBS and Dextran samples appears not to be as large as might be expected, which can be attributed to specific characteristics of the flow studied here. All experiments were conducted at steady state and intermediate flow rates, resulting at moderate pseudo-shear rates,  $\dot{\gamma} = U/h$ , where aggregation dynamics are expected to be relatively suppressed. The pseudo-shear rates in the parent branch for the present study were  $\sim 6.25 \text{ s}^{-1}$  and decreased to  $\sim 0.625 \text{ s}^{-1}$  in the daughter branch at the lowest  $Q^*$  studied. As the velocity fields in Figure 4 and the bluntness and skewness results in Figures

6 and 7 imply, the in-plane shear rate distribution in the flow would have been altered in the daughter branches. Effective shear distribution was not quantified in the present study as important information on the out of plane shearing field was not available; it is expected, however, that the out of plane shear would be greater than the in-plane shear throughout the majority of the flow field. Additionally, the regions of highest in-plane shear would be at the channel walls, where the local hematocrit is generally low. Hence, the pseudo-shear rates are probably sufficient to characterize the effective shear. These low pseudo-shear rates would suggest that there would be significant aggregation occurring in the domain. However, the transit time of the RBCs/aggregates flowing from the parent to the daughter branches was relatively small. Aggregation is a time dependent phenomenon, with a half time on the order of 5 s for normal blood samples.<sup>60,61</sup> The distance travelled along the daughter branches was approximately 0.35 mm and the average velocity in the parent branch was around 0.25 mm/s. Thus, as the flow ratio decreases, the transit time in the daughter branches increases from roughly 1.5 to 15 s. For low  $Q^*$ , and hence at the upper extreme of the transition times, it is expected that some aggregation may have occurred during data acquisition. However, from the present results it seems that, if present, this aggregation did not have sufficient time to significantly influence the velocity field.

## B. Cell-depleted layer

The increase in mean CDL thickness observed in the parent branch in the presence of aggregation is in agreement with previous studies.<sup>6,12,13,17,18,55</sup> Additionally, a number of studies have reported that at low flow rates there was a greater degree of roughness in the presence of aggregation.<sup>17,55,57</sup> The results shown in Figures 11 and 12(b) are in agreement with this result, in that the roughness was significantly greater for the Dextran case. Considering Figure 2, it can be seen why this might be the case, as deviations in the edge of the CDL are much greater for aggregates than for individual cells. This significantly increased roughness would result in increased viscous dissipation, offsetting the reduction in flow resistance which the CDL might provide.<sup>15</sup> Furthermore, the increased roughness may increase the wall shear stress by intermittently increasing the velocity gradient at the wall.<sup>57</sup> Considering the skewed CDL distributions shown in Figure 10, the deviations from the mean value would be more frequent towards the wall and hence there would be a net increase in wall shear stress. This effect may be somewhat attenuated, however, for the largest CDLs widths observed for the Dextran case at low  $Q^*$ , as increased symmetry was observed in the distribution of  $\Delta^*$  for these cases.

Additionally, it should be pointed out that the CDL was only present (to a significant level) along the inner wall of the channel. A similar asymmetry was observed by Ishikawa *et al.*<sup>29</sup> Alonso *et al.*<sup>17</sup> found that the significant asymmetry in CDL width, which occurred in their study as a result of sedimentation, increased the effective viscosity. The relative effects of the difference between the increased viscosity at the outer wall and the decreased viscosity at the inner wall require further consideration.

It was observed in Figure 9 that the probability distributions of  $\delta^*$  were generally skewed towards the wall and the modal value only moved away from the wall in the presence of aggregation in the low flow branch. The positive skewness and the wider distributions caused by aggregation are in agreement with Ong *et al.*<sup>55</sup> although in their study, the modal width was always away from the wall. This skewed distribution was also observed in the simulations of Fedosov *et al.*<sup>62</sup> Previous studies have only considered this distribution in straight vessel sections and the effect of flow ratio has not been investigated. The significant change in the shape of the distribution for low flow ratios when aggregation is present, shown in Figure 11, highlights the effect aggregation can have on the flow field.

A simple fit based on the expected distribution of cells on either side of the separating streamline was applied to Figure 12. The calculated values of the scaling parameter  $\alpha$  were found to be 0.80 and 0.51 for aggregating and non-aggregating cases, respectively. If  $\alpha$  was equal to one, it would suggest that the CDL in the parent branch was uniformly stretched across the daughter branch, whilst values smaller than one would suggest that the cells deviate from their streamlines and impinge upon the layer. The  $\alpha$  values reported above suggest that in the

aggregating cases the cells followed their streamlines fairly well, whereas for non-aggregating cases interactions between the cells resulted in a CDL width of approximately half that which would exist in the absence of cell-cell collisions. The development of larger structures in the aggregating flow reduces their freedom to move. This explanation is in agreement with Bishop *et al.*,<sup>63</sup> who found a slight decrease in the RMS deviation of cells in the presence of aggregation *in vivo*. The shape of the CDL probability distributions shown in Figure 9 for low flow ratios further supports this hypothesis. For  $Q^* = 0.1$ , as the flow exited the bifurcation, the CDL width rapidly increased, as it would if  $\alpha = 1$ . In the absence of aggregation, the distribution tends rapidly towards the vessel wall, as cell-cell interactions result in increasing impingement upon the CDL and thus depletion of its width. In the case of aggregation, the width remains relatively constant as the aggregates have less freedom of movement than individual cells. These data suggest that in the absence of aggregation, within complex geometries, CDL formation is attenuated by interactions between cells, but when the cells are aggregated, the restricted movement allows a large CDL of varying width to form. This phenomenon could potentially be used to enhance phase separation in microfluidic devices designed to extract plasma from whole blood.

### C. Inferences to *in vivo* hemodynamics

Although the present study was carried out in a rectangular channel of relatively high aspect ratio, the results can be used to infer how aggregation would affect the velocities and CDL width *in vivo* in a qualitative sense. This study has shown that aggregation not only increases the CDL width in the steady state, but also further enhances it as the flow splits between two branches. In arterioles, such branching occurs regularly and thus aggregation will further accentuate the inherent heterogeneity of the distribution of RBCs throughout the microvasculature. The constant branching of vessels in the arterioles also leads to a non-uniform velocity distribution. It has been suggested that the velocity distribution returns to uniformity after a few diameters, but that hematocrit redistribution takes around 10 diameters.<sup>58,64</sup> The present study has shown that the velocity profile can remain skewed further downstream than this. It is proposed that the CDL which forms along the inner wall of the bifurcation may be partly responsible for the observed skewness.

Due to the skewness, the velocity and hence volumetric flow of the CDL will be relatively increased and may enhance plasma skimming, should the subsequent branch happen to appear at the same location as the CDL. If a subsequent branch occurred on the opposing side to the original branch, the hematocrit in the daughter branch would be increased. Furthermore, as the flow in this branch would also be decreased (due to the skewed velocity profile), the local resistance to flow (and therefore apparent viscosity) could be increased. Across a whole microvascular bed, the specifics of the adjacent branch orientations could have a drastic impact upon the localized distributions, although regulatory mechanisms may act to maintain a relatively uniform pressure drop across the system. Current mathematical models are capable of predicting whole organ distributions of flow parameters, but are less successful on the scale of individual vessels.<sup>64,65</sup> The current study supports the hypothesis that this may be a result of the hematocrit distribution, including the CDL, in adjacent bifurcations. The amplification of the CDL width in the presence of aggregation could, therefore, have a significant impact, which may be a factor in the contradictory results reported in the literature on the effect of aggregation *in vivo*.

## V. CONCLUSIONS

Both the RBC aggregation and the cell-depleted layer are well documented phenomena in hemodynamics. However, both are geometry dependent and have been studied in either simplified geometries *in vitro*, or in highly complex geometries *in vivo*. Given the difficulties of controlling parameters and acquiring high resolution data *in vivo*, microchannel models provide an ideal domain to systematically investigate microscale blood flow. In the present study, a microchannel with a T-junction was considered. This is a very common geometrical feature in

microfluidic lab-on-a-chip devices and could also represent a microvascular bifurcation. A range of flow ratios, the proportion of flow entering the daughter branch, was considered and aggregating and non-aggregating samples of human blood were utilized.

Measurement of the cell velocity field using  $\mu$ PIV revealed velocity profiles which were skewed and sharpened at a significant distance downstream of the bifurcation. Aggregation was observed to enhance skewness but decrease the sharpening. A new methodology was developed to study the characteristics of the CDL and its variation using motion detection. This allowed for calculation of the CDL for the whole flow field. A cell-depleted layer was measured in the parent branch which was roughly doubled in width and tripled in roughness in the presence of aggregation. Downstream of the bifurcation, the CDL width was increased slightly as the proportion of flow entering the daughter branch decreased for the PBS case. However, for the Dextran case, in which aggregation was present, the CDL width increased significantly for low flow ratios. Additionally, the roughness of the surface was observed to be greatly increased by aggregation.

The steady state data from the parent branch in the present study are in general agreement with the literature in terms of the increased blunting of the velocity profiles and increased roughness and width of the CDL in the presence of aggregation. However, the geometry utilized here also allowed for high resolution information on the flow characteristics downstream of a bifurcation. This revealed how the impact of aggregation can be further amplified within the complex flow fields generated by such geometry. It is possible that this phenomenon may be of benefit in blood flow separation devices, both for plasma and white blood cells. Further work is being undertaken to elucidate the impact of aggregation in sequential bifurcations and convergences within different shear regimes and at different hematocrits.

## ACKNOWLEDGMENTS

The authors would like to thank Professor Roy Pike for the loan of equipment. Peter Vennemann for making available the PIV software JPIV ([www.vennemann-online.de](http://www.vennemann-online.de)) and Dr. D Chase and D. Johnson at King's College London Health Centre for providing use of their facilities.

- <sup>1</sup>G. Barabino, M. O. Platt, and D. Kaul, *Annu. Rev. Biomed. Eng.* **12**, 345 (2010).
- <sup>2</sup>N. Babu and M. Singh, *Clin. Hemorheol. Microcirc.* **31**, 273 (2004).
- <sup>3</sup>A. Popel, P. Johnson, M. Kameneva, and M. Wild, *J. Appl. Physiol.* **77**(4), 1790 (1994).
- <sup>4</sup>G. Cokelet, "Hemorheology and hemodynamics," in *Colloquium Series in Integrated Systems Physiology: From Molecule to Function* (Morgan & Claypool, 2011).
- <sup>5</sup>S. Chien and K. Jan, *Microvasc. Res.* **5**, 155 (1973).
- <sup>6</sup>J. Bishop, P. Nance, A. Popel, M. Intaglietta, and P. Johnson, *Am. J. Physiol. Heart Circ. Physiol.* **280**, H222 (2001).
- <sup>7</sup>M. Cabel, H. Meiselman, A. Popel, and P. Johnson, *Am. J. Physiol. Heart Circ. Physiol.* **41**, H1020 (1997).
- <sup>8</sup>M. Soutani, Y. Suzuki, N. Tateishi, and N. Maeda, *Am. J. Physiol. Heart Circ. Physiol.* **268**, H1959 (1995).
- <sup>9</sup>O. Baskurt, M. Bor-Küçükataay, and O. Yalçın, *Biorheology* **36**, 447 (1999).
- <sup>10</sup>O. Charansonney, S. Mouren, J. Dufaux, M. Duvellero, and E. Vicaud, *Biorheology* **30**, 75 (1993).
- <sup>11</sup>E. Kaliviotis and M. Yiannakis, *Clin. Hemorheol. Microcirc.* **39**, 235 (2008).
- <sup>12</sup>G. Cokelet and H. Goldsmith, *Circ. Res.* **68**, 1 (1991).
- <sup>13</sup>W. Reinke, P. Gaehtgens, and P. Johnson, *Am. J. Physiol. Heart Circ. Physiol.* **253**(3), H540 (1987).
- <sup>14</sup>S. Kim, P. Ong, O. Yalçin, M. Intaglietta, and P. Johnson, *Biorheology* **46**, 181 (2009).
- <sup>15</sup>M. Sharan and A. Popel, *Biorheology* **38**, 415 (2001).
- <sup>16</sup>B. Namgung *et al.*, *Physiol. Meas.* **31**, N61 (2010).
- <sup>17</sup>C. Alonso, A. Pries, D. Lerche, and P. Gaehtgens, *Am. J. Physiol. Heart Circ. Physiol.* **268**, H25 (1995).
- <sup>18</sup>S. Kim, R. Kong, A. Popel, M. Intaglietta, and P. Johnson, *Am. J. Physiol. Heart Circ. Physiol.* **293**, H1526 (2007).
- <sup>19</sup>A. Pries *et al.*, *Circ. Res.* **75**(5), 904 (1994).
- <sup>20</sup>S. Kim, A. Popel, M. Intaglietta, and P. Johnson, *Am. J. Physiol. Heart Circ. Physiol.* **288**, H584 (2005).
- <sup>21</sup>P. Ong *et al.*, *Physiol. Meas.* **32**, N1 (2011).
- <sup>22</sup>S. Chien, C. Tvetenstrand, M. Farrell Epstein, and G. Schmid-Schönbein, *Am. J. Physiol. Heart Circ. Physiol.* **17**(4), H568 (1985).
- <sup>23</sup>J. Dellimore, M. J. Dunlop, and P. B. Canham, *Am. J. Physiol. Heart Circ. Physiol.* **244**, H635 (1983).
- <sup>24</sup>B. Fenton, R. Carr, and G. Cokelet, *Microvasc. Res.* **29**, 103 (1985).
- <sup>25</sup>P. Gaehtgens, F. Kreutz, and K. Albrecht, *Biorheology* **15**, 155 (1978).
- <sup>26</sup>J. Perkkio, L. Wurzing, and G. Schmid-Schönbein, *Thromb. Res.* **45**, 517 (1987).
- <sup>27</sup>V. Doyeux, T. Podgorski, S. Peponas, M. Ismailand, and G. Coupiat, *J. Fluid Mech.* **674**, 359 (2011).
- <sup>28</sup>V. Leble *et al.*, *Biomicrofluidics* **5**, 044120 (2011).
- <sup>29</sup>T. Ishikawa *et al.*, *Biomed. Microdevices* **13**, 159 (2011).
- <sup>30</sup>J. Chesnutt and J. Marshall, *Microvasc. Res.* **78**, 301 (2009).

- <sup>31</sup>R. Lima, S. Wada, K. Tsubota, and T. Yamaguchi, *Meas. Sci. Technol.* **17**, 797 (2006).
- <sup>32</sup>D. Long, M. Smith, A. Pries, K. Ley, and E. Damiano, *Proc. Natl. Acad. Sci. U.S.A.* **101**(27), 10060 (2004).
- <sup>33</sup>P. Vennemann *et al.*, *J. Biomech.* **39**, 1191 (2006).
- <sup>34</sup>S. Wereley and C. Meinhart, *Annu. Rev. Fluid Mech.* **42**, 557 (2010).
- <sup>35</sup>J. Hove *et al.*, *Nature* **421**, 172 (2003).
- <sup>36</sup>A. Nakano, Y. Sugii, M. Minamiyama, and H. Niimi, *Clin. Hemorheol. Microcirc.* **29**, 445 (2003).
- <sup>37</sup>J. Dusting, E. Kaliviotis, S. Balabani, and M. Yianneskis, *J. Biomech.* **42**, 1438 (2009).
- <sup>38</sup>E. Kaliviotis, J. Dusting, and S. Balabani, *Med. Eng. Phys.* **33**(7), 824 (2011).
- <sup>39</sup>C. Zhao and X. Cheng, *Biomicrofluidics* **5**, 032004 (2011).
- <sup>40</sup>H.-W. Wu, C.-C. Lin, and G.-B. Lee, *Biomicrofluidics* **5**, 013401 (2011).
- <sup>41</sup>S. Hur, A. Mach, and D. Di Carlo, *Biomicrofluidics* **5**, 022206 (2011).
- <sup>42</sup>M. Faivre, M. Abkarian, K. Bickraj, and H. Stone, *Biorheology* **43**, 147 (2006).
- <sup>43</sup>M. Kersaudy-Kerhoas, R. Dhariwal, M. Desmulliez, and L. Jouvet, *Microfluid. Nanofluid.* **8**, 105 (2010).
- <sup>44</sup>E. Sollier, H. Rostaing, P. Pouteau, Y. Fouillet, and J. Achard, *Sens. Actuators B* **141**, 617 (2009).
- <sup>45</sup>S. Yang, A. Undar, and J. Zahn, *Lab Chip* **6**, 871 (2006).
- <sup>46</sup>M. Pearson and H. Lipowsky, *Microcirculation* **11**, 295 (2004).
- <sup>47</sup>R. Kuczenski, H.-C. Chang, and A. Revzin, *Biomicrofluidics* **5**, 032005 (2011).
- <sup>48</sup>I. Sarelius and B. Duling, *Am. J. Physiol. Heart Circ. Physiol.* **12**, H1018 (1982).
- <sup>49</sup>J. Westerweel and F. Scarano, *Exp. Fluids* **39**, 1096 (2005).
- <sup>50</sup>H. Bruus, *Theoretical Microfluidics* (Oxford University Press, 2008).
- <sup>51</sup>F. Gijzen, F. van de Vosse, and J. Janssen, *J. Biomech.* **32**, 601 (1999).
- <sup>52</sup>S. Chen, B. Gavish, S. Zhang, Y. Mahler, and S. Yedgar, *Biorheology* **32**(4), 487 (1995).
- <sup>53</sup>A. Koutsiaris, *Clin. Hemorheol. Microc.* **43**, 321 (2009).
- <sup>54</sup>G. Tangelder *et al.*, *Circ. Res.* **59**, 505 (1986).
- <sup>55</sup>P. Ong, B. Namgung, P. Johnson, and S. Kim, *Am. J. Physiol. Heart Circ. Physiol.* **298**, H1870 (2010).
- <sup>56</sup>S. Kim, R. Kong, A. Popel, M. Intaglietta, and P. Johnson, *Microcirculation* **13**, 199 (2006).
- <sup>57</sup>B. Namgung, P. Ong, P. Johnson, and S. Kim, *Ann. Biomed. Eng.* **39**(1), 359 (2011).
- <sup>58</sup>A. Pries, K. Ley, M. Claassen, and P. Gaehtgens, *Microvasc. Res.* **38**, 81 (1989).
- <sup>59</sup>B. Das, P. Johnson, and A. Popel, *Biorheology* **35**(1), 69 (1998).
- <sup>60</sup>E. Kaliviotis and M. Yianneskis, *Biorheology* **45**, 639 (2008).
- <sup>61</sup>G. Cokelet, *Annu. Rev. Physiol.* **42**, 311 (1980).
- <sup>62</sup>D. Fedosov, B. Caswell, A. Popel, and G. Karniadakis, *Microcirculation* **17**, 615 (2010).
- <sup>63</sup>J. Bishop, A. Popel, M. Intaglietta, and P. Johnson, *Am. J. Physiol. Heart Circ. Physiol.* **283**, H1985 (2002).
- <sup>64</sup>G. Cokelet, *Biorheology* **36**, 343 (1999).
- <sup>65</sup>A. Pries, T. Secomb, P. Gaehtgens, and J. Gross, *Circ. Res.* **67**, 826 (1990).